

Defect Sizing, Distance and Substrate Effects in Ion-Irradiated Monolayer 2D Materials

Pierce Maguire,^{1,2} Daniel S. Fox,^{1,2} Yangbo Zhou,^{1,2,3} Qianjin Wang,⁴ Maria O'Brien,^{2,5} Jakub Jadwiszczak,^{1,2} John McManus,^{2,5} Niall McEvoy,^{2,5} Georg S. Duesberg,^{2,5,6} and Hongzhou Zhang^{1,2,*}

¹*School of Physics, Trinity College Dublin, Dublin 2, Ireland*

²*AMBER Centre, CRANN Institute, Trinity College Dublin, Dublin 2, Ireland*

³*School of Material Science and Engineering, Nanchang University, Youxun W Rd, Xinjian Qu, Nanchang Shi, Jiangxi Sheng, People's Republic of China*

⁴*National Laboratory of Solid State Microstructures, Nanjing University, Nanjing 210093, Jiangsu Province, People's Republic of China*

⁵*School of Chemistry, Trinity College Dublin, Dublin 2, Ireland*

⁶*Institute of Physics, EIT 2, Faculty of Electrical Engineering and Information Technology, Universität der Bundeswehr München, Werner-Heisenberg-Weg 39, 85577 Neubiberg, Germany*

(Dated: July 21, 2022)

Precise, scalable, defect engineering of 2D nanomaterials is acutely sought after in contemporary materials science. Here we present defect engineering in monolayer graphene and molybdenum disulfide (MoS₂) by irradiation with noble gas ions at 30 keV. Two ion species of vastly different mass were used in a gas field ion source microscope: helium (He⁺) and neon (Ne⁺). A detailed study of the introduced defect sizes and interdefect distance with escalating ion dose was performed using Raman spectroscopy. Expanding on existing models, it is found that the average defect size is considerably smaller for supported than freestanding graphene and that the rate of defect production is larger. It is concluded that secondary atoms from the substrate play a significant role in defect production, creating numerous smaller defects rather than those created by the primary ion beam.

Furthermore, a model was also applied to supported MoS₂, another promising member of the 2D material family. Corrective factors for both ions were obtained for MoS₂, demonstrating their different behaviour and facilitating comparison with other irradiation conditions in literature.

Keywords: Gas field ion microscope, helium ion, neon ion, focused ion beam, graphene, molybdenum disulfide, 2D materials, Raman spectroscopy, defect engineering

I. INTRODUCTION

IN recent years, the extraordinary properties and tunability of 2D materials have been repeatedly demonstrated, heralding a new era of materials science.^{1,2} The physical properties (electrical, thermal, etc.) of 2D materials are highly distinguished with respect to their bulk counterparts due to their evolution of band structure with layer number.³⁻⁶ The ideas and methodologies developed from the investigation of graphene have been extended to many other 2D materials, including transition metal dichalcogenides (TMDs) such as molybdenum disulfide (MoS₂).^{7,8}

The alteration of nanoscale geometry and the introduction of structural defects or strain to these materials can be used to modulate their electronic and optical properties.⁹⁻¹⁵ Ion irradiation has an illustrious record over many decades in the scalable, precise defect-engineering of materials.¹⁶ With the demands of modern semiconductor technology, precise nanoscale control of 2D material properties is fervently sought after and eminently achievable using modern ion irradiation techniques with sub-nanometre probe sizes.¹⁷⁻²² Given the superlative confinement of such materials, it is possible to restrict the ion-induced interaction to an exceptionally small region. Such methods have been used to create nanoribbons with widths of less than 10 nm, control doping by implantation and introduce precise quantities

of defects.^{14,19,23-25} He⁺ irradiation of graphene encapsulated in hexagonal boron nitride has even been used to introduce n-type doping.²⁶

The ion species and energies used in this work are particularly significant due to their high resolution capability for nanofabrication and complementary precise defect engineering. Given the pivotal importance of defect engineering and nanofabrication methods in the materials science of today, it is imperative that the effects of these ion beam fabrication methods on 2D materials be well understood. In short, the irradiation methods must be related to both defect number (interdefect distance) and size. While a comparison of defect sizes introduced by energetic noble gas ions in graphene has been performed using molecular dynamics, this is (to the authors' knowledge), the first experimental comparison for graphene. It is also one of very few reports to distinguish between supported and freestanding graphene which, as the results indicate, is expected to be of critical importance to the manufacture of graphene based electronics using ion methods.

In graphene, the defect yield and the nature of defects introduced by these ion species are inferred from Raman spectra using established models^{13,14,27}. A similar model is applied to MoS₂ which does not provide the same level of information but it is expected that these results will inform future work²⁴.

A. Graphene Background

The Raman spectra of carbon materials and their alteration by irradiation techniques have been extensively studied.^{13,14,25,28-32} The following characteristic peaks appear in graphene spectra: $2D$ at ~ 2640 cm^{-1} and G at ~ 1583 cm^{-1} . In the Raman spectra of defective graphene, the disruption to normal Raman selection rules also allows the detection of two further peaks, particularly as the average distance between defects, L_D , decreases: D at ~ 1322 cm^{-1} , and D' at ~ 1600 cm^{-1} .^{28,33} L_D in graphene has been related to the ratio of the intensity of the D peak (I_D) to the intensity of the G peak (I_G) by Lucchese *et al.* and a version is given here by:¹³

$$\frac{I_D}{I_G} = C_A \frac{(L_S^2 + 2r_S L_S)}{(L_S^2 + 2r_S L_S - r_S^2)} \left[e^{-\pi r_S^2 / L_D^2} - e^{-\pi(L_S^2 + 2r_S L_S) / L_D^2} \right] + C_S \left[1 - e^{-\pi r_S^2 / L_D^2} \right] \quad (1)$$

The average size of a region surrounding a defect created by the ion beam is described by two radii: r_S is the radius of the structurally disordered area and r_A is the radius surrounding the point defect in which D scattering occurs. $L_S = r_A - r_S$ is the Raman relaxation length for the resonant Raman scattering. The intensity of the D peak is proportional to the total area of crystalline graphene that is activated by local defects, not the area of the defects themselves. Thus, as L_D becomes sufficiently low and the material becomes less crystalline, the D band intensity falls. The effect of the excitation energy, E_i , on the ratio of excitation of the D and G bands, is included in the C_A parameter. C_A has been given experimentally by:¹⁴

$$C_A = (160 \pm 48) \times E_i^{-4} \quad (2)$$

The C_S parameter is the value of the I_D/I_G ratio in the highly disordered limit and it is important only in the large defect density regime, $L_D \leq r_S$.^{13,14} Typically, three stages are discussed in the evolution of the relationship described by equation 1. The first stage begins with pristine graphene (having a very large L_D) and as disorder is increased, a rising D peak may be observed, increasing I_D/I_G . In addition, a broadening of all peaks occurs. It can be attributed to isolated defects initially appearing in a crystalline lattice. The second stage features a now diminishing D peak and the continued broadening and newly observed redshifting of the G peak. It is reached when L_D reaches a critical quantity such that defect coalescence is significant. The second stage can be attributed to the now dominant effect of a declining number of six-atom carbon rings present.^{13,14,25,32} The third stage is not described in detail here as it is in essence marked by the transition of the specimen to amorphous carbon bearing limited or no resemblance to the original graphene.

B. MoS₂ Background

Similarly for MoS₂, the evolution of its Raman spectra with decreasing L_D has been described by Mignuzzi *et al.* as follows:²⁴ The intensity of the $LA(M)$ peak, $I(LA)$, normalized to that of either the E' peak, $\frac{I(LA)}{I(E')}$, or the A'_1 peak, $\frac{I(LA)}{I(A'_1)}$, is related to the inverse square of L_D by equation 3:

$$\frac{I(LA)}{I(X)} = \frac{C(X)}{L_D^2} \quad (3)$$

where $X = E'$ or A'_1 and $C(E') = 1.11 \pm 0.08$ nm^2 and $C(A'_1) = 0.59 \pm 0.03$ nm^2 . With rising disorder, the increase of these intensity ratios is attributed to two concomitant factors: (i) an increase in the absolute intensity of the defect activated LA(M) peak, and (ii) a decrease in the intensity of the E' and A'_1 peaks that is possibly due to the ablation of the specimen.²⁴

II. EXPERIMENT

A. Sample Preparation

1. Graphene

Chemical vapour deposition (CVD) was used to grow the graphene sample which was then transferred to a Si substrate as outlined in literature.³⁴

2. MoS₂

CVD MoS₂ was prepared using a previously described technique.³⁵ MoO₃ precursor substrates were placed face-up in a ceramic boat with a blank substrate face down on top of this. This was then placed in the centre of the heating zone of a quartz tube furnace, and ramped to 750°C under 150 SCCM of Ar flow. Sulfur (S) vapour was then produced by heating S powder to 120°C in an independently controlled upstream heating zone of the furnace, and carried downstream to the MoO₃ for a duration of 20 min after which the furnace was held at 750 °C for 20 min, then cooled down to room temperature.

B. Irradiation

The ORION NanoFab microscope was used to irradiate arrays of 5×5 μm regions in graphene and 3×3 μm regions in MoS₂ with He⁺ and Ne⁺ at an energy of 30 keV and at an angle of incidence of 0°. These regions received doses ranging from 1.5×10^{11} to 1×10^{16} Ne⁺ cm^{-2} or 1×10^{13} to 1×10^{17} He⁺ cm^{-2} . The regions were found using low dose, low magnification He⁺ imaging. He⁺ was chosen to minimise damage to the sample and utilise its

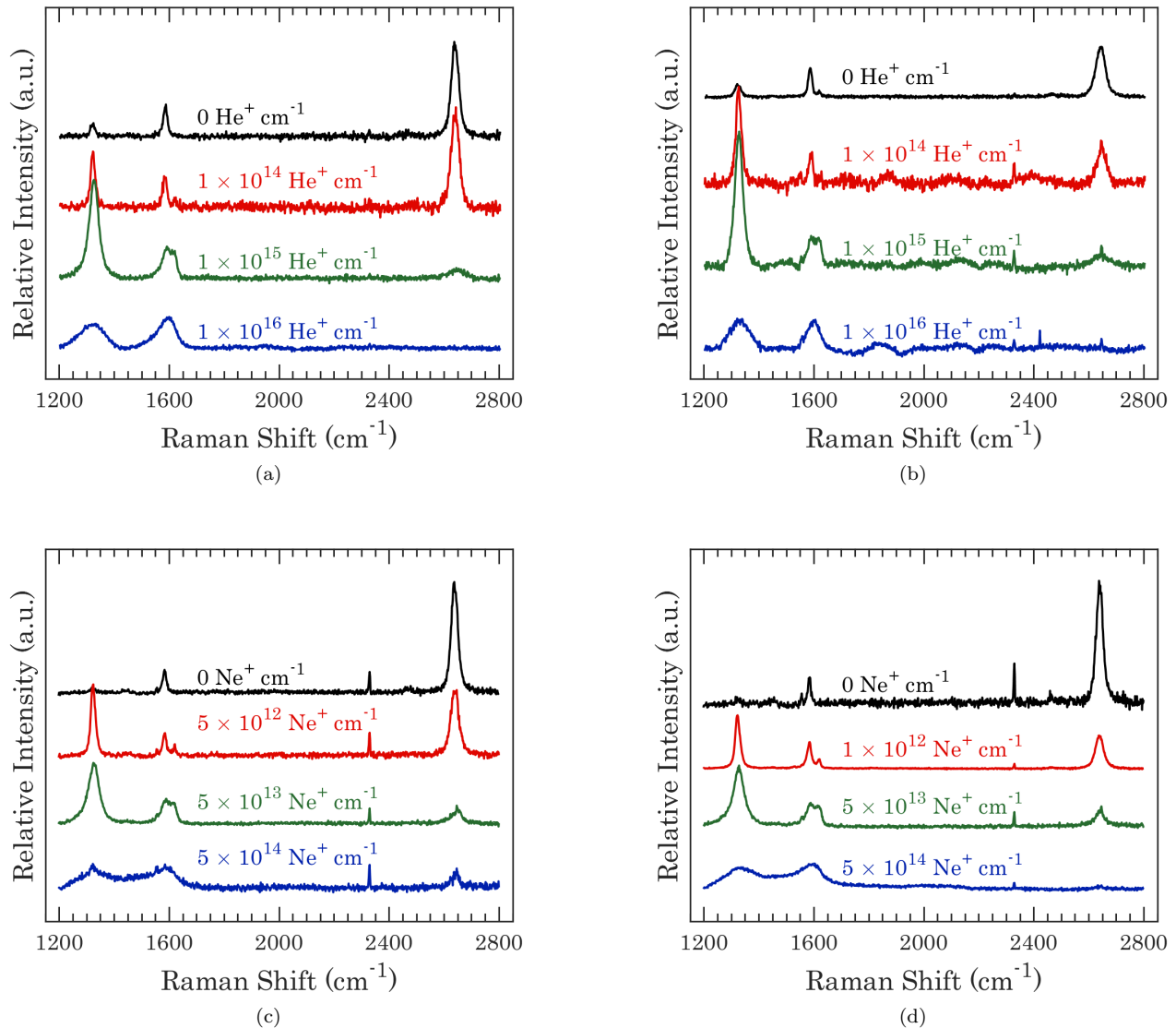


FIG. 1. Representative selection of graphene Raman spectra excited by a 633 nm laser and irradiated with ions at 30 keV with a 0° angle of incidence. (a) freestanding graphene irradiated with He^+ , (b) supported graphene irradiated with He^+ , (c) freestanding graphene irradiated with Ne^+ , (d) supported graphene irradiated with Ne^+ . The evolution of the spectra with increased ion dose is shown descending from the top in black to the bottom in blue. The spectra are normalised to the maximum of the G peak.

superior imaging quality. A low dose was carefully ensured (less than $1 \times 10^{10} \text{ He}^+ \text{ cm}^{-2}$ total from imaging). Once the desired region was located on the specimen, the desired ion species was selected. The beam was slightly defocused to ensure a uniform distribution of ions and the sample was irradiated at the desired dose. A 1 pA beam current and 10 nm pixel spacing were used. The beam dwell time at each pixel and/or the number of repeats at each position were varied to achieve the desired dose.

C. Raman Spectroscopy

Raman spectra were acquired from each irradiated region and from a nearby non-irradiated region for reference. Raman spectroscopy was carried out on graphene with a Horiba Jobin-Yvon ($\lambda_L=633 \text{ nm}$) laser with a 1200 lines/mm diffraction grating. There is a small artifact peak at $\sim 2330 \text{ cm}^{-1}$ apparent in the spectra which is believed to arise from the tool or environment. These spectra were acquired from a single point for each region. Raman spectroscopy was carried out on MoS_2 using a Witec alpha 300R with a 532 nm excitation laser

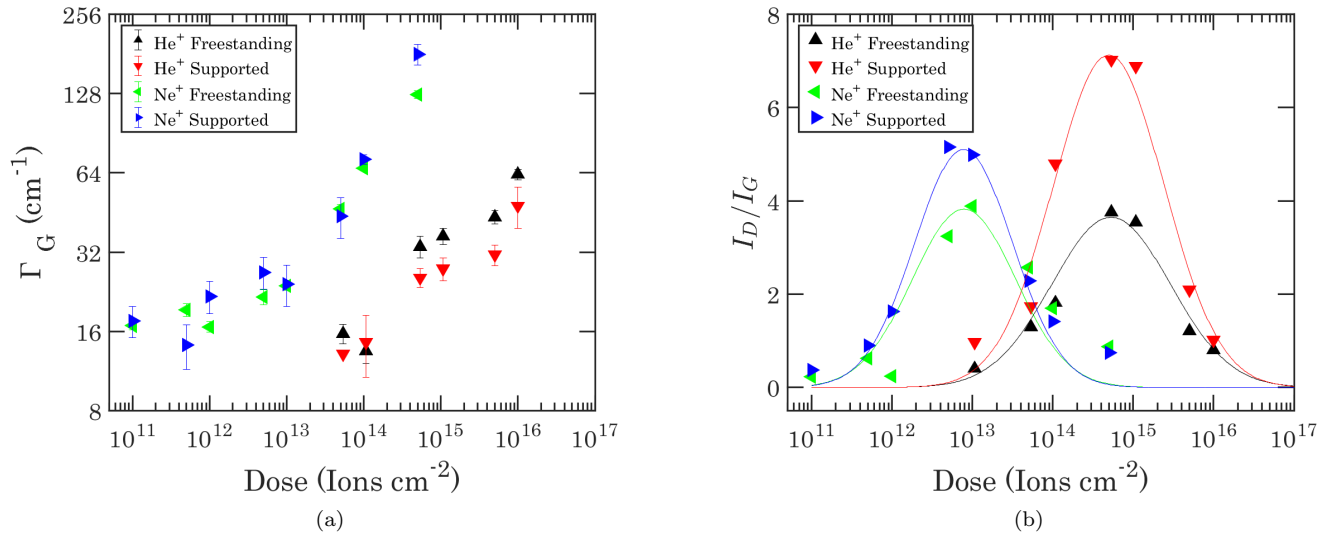


FIG. 2. (a) Evolution of full width at half maximum of Lorentzian fits to the G peak, Γ_G , as a function of dose for He⁺ and Ne⁺ for both freestanding and supported graphene. (b) The evolution of the I_D/I_G ratio of graphene with irradiation dose. A Gaussian function has been fitted to each of the four data sets in this graph for illustrative purposes only.

with a 1800 lines/mm diffraction grating. These spectra were acquired from the desired region by averaging the relevant area of an acquired map. For both materials, the laser power was around 1 mW or less to minimise damage to the samples. Peaks in the Raman spectra of graphene were fitted with Lorentzian functions using the fityk software package as these were found to fit the spectra most closely.³⁶ Error bars, where used and unless otherwise stated, are the largest of either the instrumental (1 cm^{-1}) or the fitting error as acquired from fityk which uses a weighted sum of squared residuals to measure agreement between the fit and the data.³⁷

III. RESULTS & DISCUSSION

A. Graphene

In figures 1(a)-(d), four sets of Raman spectra, with intensity as a function of Raman shift are presented in each. The spectra obtained from the non-irradiated regions of both supported and freestanding samples are shown in black and agree with values from literature for monolayer graphene as stated in section IA.^{28,30} However, the spectra do not represent completely pristine graphene. This variation is not expected to be important due to the magnitude of change affected by the ion beam being far greater. Further discussion of the monolayer but non-pristine starting material is provided in the supplementary information for reference.

In each figure, multiple spectra are shown, descending with increased ion dose. Evolution through the previously discussed stages is illustrated as follows: The first

spectrum (black) represents the non-irradiated graphene; the second spectrum (red), represents the first stage, where the defect activated D peak can be observed to have increased in intensity at $\sim 1322 \text{ cm}^{-1}$; the third spectrum (green) cannot be assigned unambiguously to a stage, but it is approximately at the end of the first or the beginning of the second stage as evidenced by the D peak being close to its maximum; finally, the fourth spectrum (blue) represents the third stage. Here the highest ion dose was applied, and the Raman spectra have now been altered such that the material is amorphous carbon with little to no remaining crystallinity.

The width of the G peak increases as a function of ion dose as shown in figure 2(a) for both He⁺ and Ne⁺. With increasing dose, the G peak is observed to consistently broaden and decrease in intensity, representing an unequivocal increase in structural disorder. Given their increased mass, Ne⁺ ions have an enhanced milling capability at the incident surface compared to He⁺, and here the effect of using the heavier Ne⁺ instead of He⁺ at the same energy is highly pronounced.³⁸ While the trends are similar, the incidence of the Ne⁺ species causes evolution of the G peak to occur at ion doses which are lower by between one and two orders of magnitude.

In figure 2(b), the evolution of the I_D/I_G ratio against dose is displayed for both He⁺ and Ne⁺ and for both freestanding and supported graphene. The three stages previously outlined are observed. I_D/I_G of the supported graphene is noted to rise faster and reach a much higher maximum than the freestanding material. This is discussed further in relation to defect sizes later. To aid the understanding of these results, the interaction of the ions upon incidence with the specimens must be considered.

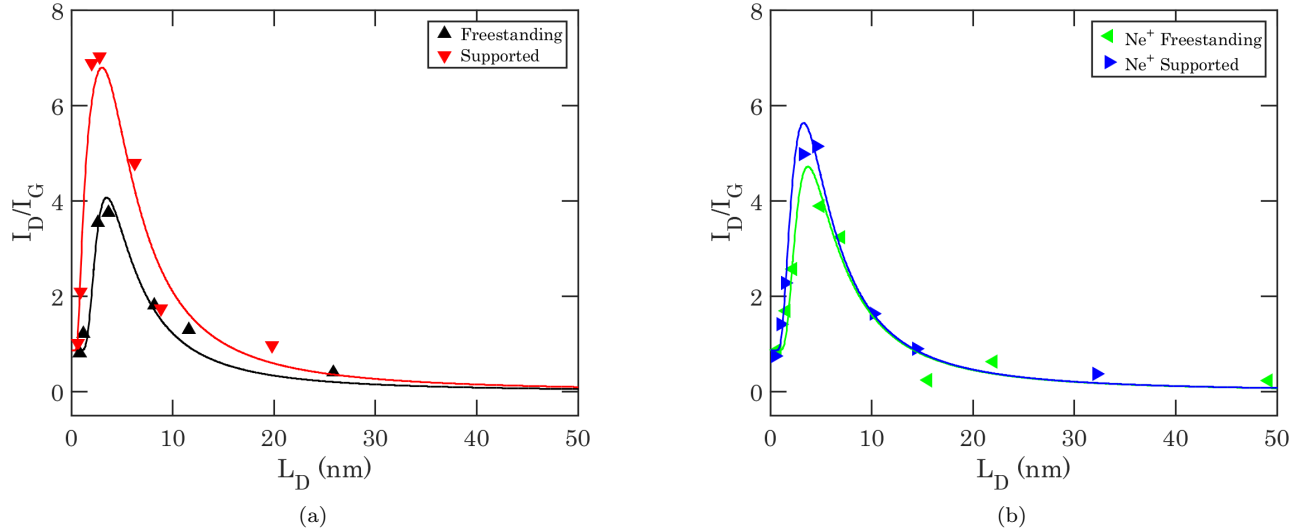


FIG. 3. The evolution of the I_D/I_G ratio of freestanding and supported graphene with L_D for (a) He^+ and (b) Ne^+ . The points represent experimental data and the lines are from a non-linear fit of l^{13} .

Ion	Graphene	$\gamma_{C(SRIM)}$	$\gamma_{C(MD)}$	$\alpha_{C(fit)}$
He^+	Freestanding	0.010	0.006	0.016
He^+	Supported	0.137	–	0.027
Ne^+	Freestanding	0.236	0.156	0.414
Ne^+	Supported	3.15	–	0.965

TABLE I. Sputtering yields and defect per incident ion values of carbon (atoms/ion) from graphene irradiated with He^+ and Ne^+ at 30 keV and 0° angle of incidence for the four different arrangements discussed in the main text. $\gamma_{C(SRIM)}$ is calculated using SRIM, $\gamma_{C(MD)}$ is calculated using the online simulation code from Lehtinen *et al.* and $\alpha_{C(fit)}$ is calculated from the fits shown in figure 3.^{39,40}

Sputtering is the removal of near-surface atoms from a target, and the sputtering yield is the mean number of sputtered target atoms per incident ion. Irradiation induced defects in graphene come from two main divisions: those introduced directly by the ion beam and, in the case of supported samples, there are also defects introduced indirectly by the interaction of backscattered primary particles and secondary sputtered substrate atoms.⁴¹ Such atoms have a much lower energy and therefore a much higher cross section for sputtering interaction with the carbon atoms at the surface. These collisions occur to a far greater extent for supported material where the substrate both facilitates backscattering of the primary ion beam and provides a source of secondary atoms.⁴¹ For high energy ions, a substrate is expected to increase the rate of damage per ion given the supply of secondary atoms and backscattered ions. For low energy ions, a substrate is expected to greatly lower the damage probability per ion. Zhao *et al.* found that the energies above which irradiation damage was en-

hanced in supported graphene were 5 keV and 3 keV for Ar^+ ($M=18$) and Si^+ ($M=14$) respectively.⁴¹

The sputtering yields of graphene were calculated using stopping and range of ions in matter (SRIM) simulations ($\gamma_{C(SRIM)}$) as detailed in the experimental section.^{42–44} SRIM is not expected to be quantitatively accurate for ion-nanomaterial systems where molecular dynamics is a superior, albeit far more computationally expensive choice.^{39,45–47} In calculating the yield of carbon atoms from graphene, SRIM accounts for those carbon atoms removed directly by the primary ion beam and those which are removed by backscattered primary ions. The sputtering yields of both ions when interacting with the sample (both freestanding and supported) are shown in table I. The four scenarios applied in experiment were also simulated: (i) freestanding, irradiated with He^+ , (ii) supported, irradiated with He^+ , (iii) freestanding, irradiated with Ne^+ , and (iv) supported, irradiated with Ne^+ . As can be seen in table I, the sputtering yields calculated using SRIM for each ion are much larger for supported than freestanding graphene. The effects of secondary atoms from the substrate and, to a lesser extent, ions backscattered by it are thus expected to have a significant impact on the rate of defect introduction to the graphene layer. Nonetheless, SRIM was used to provide initial estimates of sputtering yields for an iterative fit of equation 1 to experimental data. Values calculated using molecular dynamics are also presented in table I. These were calculated from the work of Lehtinen *et al.* who investigated the effects of different ion species on the incidence of single vacancy, double vacancy and other more complex defect types in freestanding graphene.³⁹

In the previous work of Lucchese *et al.*, low energy (90 eV) Ar^+ ions were used to alter L_D in graphene

which was investigated using Raman spectroscopy.¹³ This study provided a model with which to quantify defects in graphene. Cançado *et al.* expanded the model to multiple Raman excitation energies.¹⁴ In these studies, L_D was calculated based on the expected density of defects, σ , which is estimated from the irradiation dose, S , in ions per nm^{-2} . The approximation that $\sigma \simeq S$ was used which assumes a random distribution of ions, yielding

$$L_D = 1/\sqrt{\sigma} \quad (4)$$

^{13,24,25} This is a valid assumption for ions with a suitable cross-section for creating a single carbon vacancy defect. The 90 eV Ar^+ ions applied to graphene by Lucchese *et al.* are one such example due to their relatively large mass and low energy. The vast majority of ions do indeed interact with surface carbon atoms but due to the low energy can only remove one carbon atom each. However, in this work the irradiation species are much lighter and at much higher energies than those used by Lucchese *et al.*, making this assumption no longer valid. The dose used to calculate L_D must be corrected by the probability of creating a defect (i.e. the number of D band active zones created per ion), α_C , so that $\sigma\alpha_C \simeq S$ and thus:

$$L_D = 1/\sqrt{\sigma\gamma_C} \quad (5)$$

α_C is distinguished from the sputtering yield of carbon from graphene, γ_C , because not all defects causing D band activation need necessarily be a vacancy. However, γ_C , is easily calculated as a useful reference and is used as a seed value for α_C in fitting.

1. Defect Probabilities

The process of fitting a form of equation 1 to our data involved using initial values from previous studies. The process is described in detail in the supplementary information. The fits of equation 1 are applied to the four data sets in 3(a) and (b), showing the close agreement of the experimental data and the fitted equation. The values for α_C obtained by fitting, $\alpha_{C(\text{fit})}$, are shown in table I alongside their corresponding seed values found using SRIM, $\gamma_{C(\text{SRIM})}$, and those found using the molecular dynamics-derived method of Lehtinen *et al.*, for freestanding graphene only, $\gamma_{C(\text{MD})}$.⁴⁰ The sputtering yield of He^+ on freestanding graphene has also been measured experimentally before using a single pixel exposure to completely mill through a graphene layer.⁴⁸ The value reported by Buchheim *et al.* is $\gamma_C = 0.007$, which is in close agreement with atomistic simulations.⁴⁸ Given that this figure neglects defects that do not involve sputtering, it is expectedly smaller than the value of α_C obtained in this work. Similarly, in the case of Ne^+ on freestanding graphene, we obtain a value of α_C which is more than twice the value of γ_C from molecular dynamics. In freestanding graphene, the dominant defect introduction process is expected to be the interaction of

the direct ion beam. However, in supported graphene this is in conjunction with defects introduced by low energy secondary atoms which have been sputtered from the substrate. The obtained result, that α_C is consistently larger for supported than freestanding graphene, is thus in keeping with expectations.

2. Defect Sizes

It is noted that the maximum I_D/I_G value is considerably higher for supported graphene than for freestanding graphene. It is observed from equation 1 and demonstrated in figure S1 in the supplementary information that there is a negative linear relationship between r_S and the I_D/I_G ratio. Depending on many factors, but principally the irradiation species, energy and angle, we can generally expect r_S values between approximately 0.8 and 2.5 nm.^{25,49} It has been established that larger incident species generally produce larger defects.^{25,39,40} However, in the freestanding case, r_S is unexpectedly not found to be larger for Ne^+ than He^+ , despite the very different ion mass. This He^+ behaviour may be related to a similarly unexpected experimental finding by Gawlik *et al.*⁴⁹. Also observable are the substantially higher values for r_S for freestanding than supported graphene. Lehtinen *et al.* found that the size of defects introduced by the direct ion beam typically increases with ion energy.³⁹ While the high energy interaction of the direct beam is expected to be causing large defects, it also energises lower energy atoms which in turn produce numerous, smaller graphene defect sites.

For supported graphene irradiated with 30 keV He^+ , r_S has been found to be ~ 0.8 -1 nm.^{21,32} The value obtained in this work for He^+ is slightly smaller than previous reports.^{21,32} Since the mass of Ne^+ is between those of He^+ and Ga^+ , by a simple argument, it might be expected that the corresponding r_S value would be similarly intermediate. Although unclear in the case of freestanding experiments as previously discussed, this is indeed true for supported graphene. Ga^+ , also incident on supported graphene and also at 30 keV, has been reported to create defects of $r_S = 1.6 \text{ nm}$ ²¹. Thus the trend for supported graphene is clearly one of increasing defect size (with increasing ion mass, m_a):

Ion	r_S	m_a
He^+	0.68 nm	4
< Ne^+	1.12 nm	20.1
< Ga^+	1.6 nm	9.7 ²¹

It is proposed that the larger ion transfers energy more efficiently to substrate atoms (the masses of Si and Ne are very close), and it is these atoms, being more energised than their He^+ induced counterparts, which create larger defects in the graphene layer. The variety of r_S values obtained in this work suggest a variety of defect types with different weighting in the four different experimental scenarios. Such defects may include single vacan-

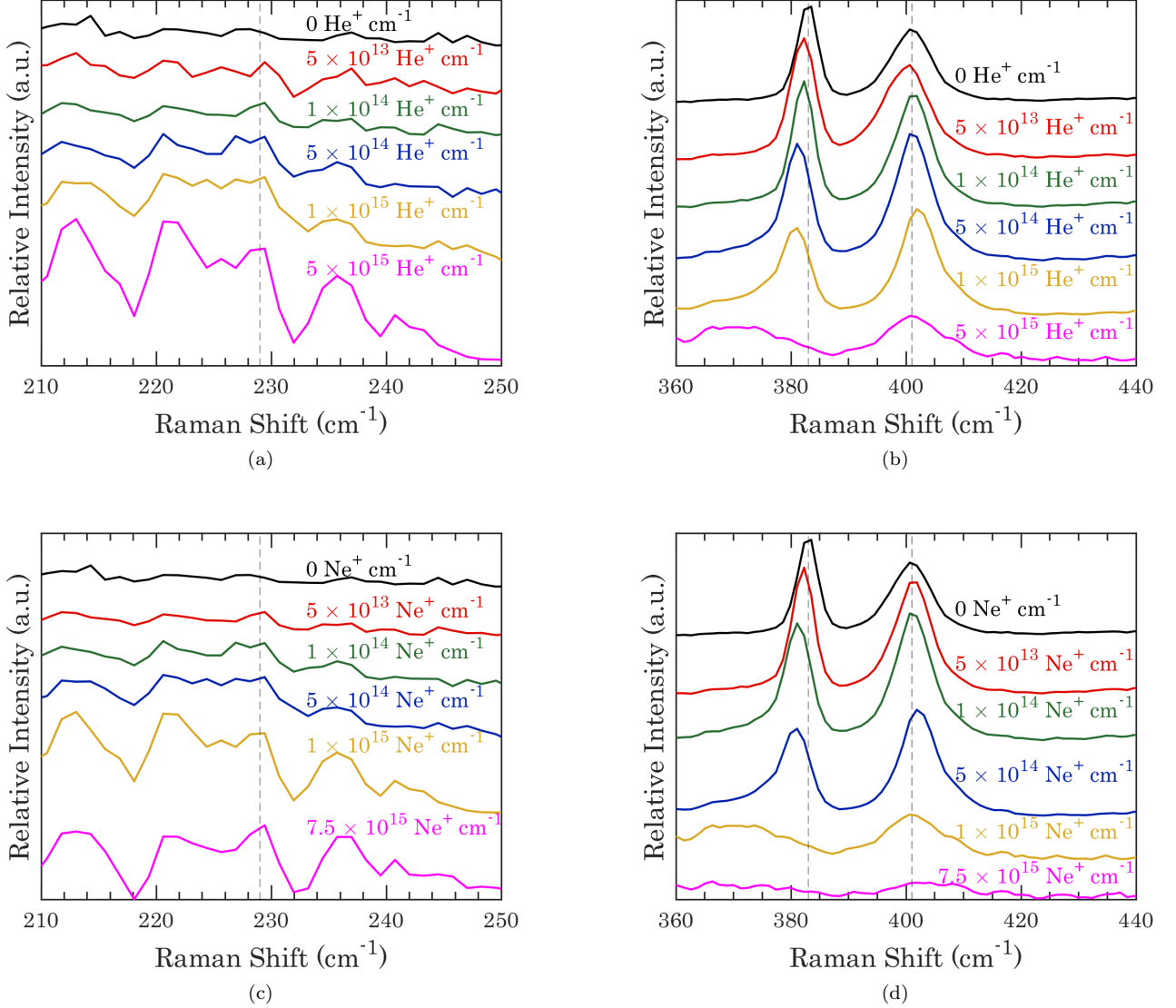


FIG. 4. A representative selection of Raman spectra of MoS₂ with increased ion doses descending from pristine at the top (in black) to highest dose at the bottom (in magenta). MoS₂ irradiated with He⁺ is shown in (a) and (b) and Ne⁺ in (c) and (d) at 30 keV. (a) and (c) show the region surrounding the LA(M) mode at $\sim 229\text{cm}^{-1}$ while (b) and (d) show the region surrounding the E' and A'_1 peaks. A 533 nm laser was used as the excitation source.

cies, double vacancies, complex defects or amorphisation events.^{39,40} It underscores the importance of choosing ion and substrate carefully for both nanofabrication and defect engineering.

B. MoS₂

To expand our study to reflect the wide variety of 2D materials being modified with ion beams, monolayer MoS₂ which was synthesised by a previously reported CVD technique was also investigated.³⁵ In figures 4 (b,d), the characteristic E' and A'_1 peaks of monolayer MoS₂

Ion	Graphene	r_S	r_A	$L_D \left(\frac{I_D}{I_G}\right)_{max}$	$\left(\frac{I_D}{I_G}\right)_{max}$
He ⁺	Free	1.83	2.93	3.48	3.93
He ⁺	Supp	0.68	2.81	2.75	6.47
Ne ⁺	Free	1.62	3.19	3.70	4.72
Ne ⁺	Supp	1.12	3.02	3.28	5.64

TABLE II. Key figures including r_S , the average defect size, calculated from fitting equation 1 to graphene experimental data as in figure 3.

are marked by dark grey dashed lines. They are clear in the pristine spectra (in black) and are in good agree-

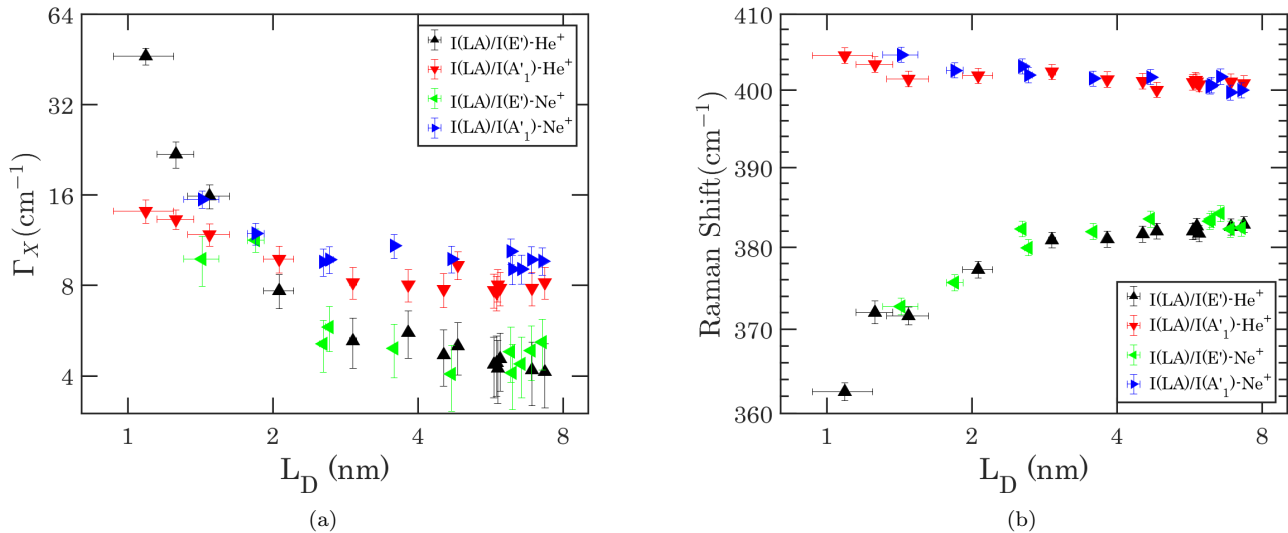


FIG. 5. The evolution of (a) FWHM (Γ_X) of MoS₂ Raman modes and (b) peak position with calculated L_D .

ment with literature. The E' peak, visible at $\sim 383 \text{ cm}^{-1}$ comes from the intra-layer, in-plane motion of Mo and S atoms with respect to each other. The A'_1 peak at $\sim 401 \text{ cm}^{-1}$ comes from the intralayer, out of plane motion of S atoms.^{8,50-54} The small separation of these two peaks, $\sim 18 \text{ cm}^{-1}$, is indicative of monolayer MoS₂. With increasing ion dose, reductions in intensity and broadening of these two characteristic peaks are observed. This reflects the growing disorder which the ion beams create in the material. To examine the spectra in greater detail, Gaussian peaks were fitted to the spectra and their parameters compared. The evolutions of peak width and peak position of the E' and A'_1 peaks are shown in figure 5 (a) and (b) respectively. Both peaks are observed to broaden with increasing disorder. The onset of broadening occurs at a substantially lower dose for He⁺ than for Ne⁺, although the trend has a similar shape as expected. The most dramatic change with increasing dose of both ions is the red shift of the E' peak. This downward shift in energy is attributed to the introduction of defects causing lattice distortion, reflected in the Raman spectrum similarly to tensile strain.^{8,50,55-58} Changes in the position of the peak of the A'_1 peak are considerably lower in magnitude, although it does blue shift for some of the higher doses used, as previously reported.²⁴

In figures 4 (a,c), a different range of the same spectra is presented. It shows the emergence of a new peak particularly at high doses. This peak at $\sim 229 \text{ cm}^{-1}$ (dashed grey line) in our spectra has been labelled as the LA(M) mode⁵⁹. Mignuzzi *et al.* drew an analogy between the LA(M) peak in MoS₂ and the D peak in graphene as both are defect-activated and when normalised represent a good measure of disorder²⁴.

Mignuzzi *et al.* used equation 3 to describe the effect of introducing defects on the Raman spectrum of MoS₂.²⁴

This equation and the constants provided previously were used to calculate the corresponding average displacement between defects from experiment $L_{D(exp)}$ for both peaks. The average value from both the E' and the A'_1 peaks was then calculated for each ion species. It is this value which is used on the x-axis of figures 6 (a) and 5 (a),(b).

The estimated average displacement between defects from the assumption that one ion causes one defect, $L_{D(est)}$, was also obtained using equation 4. In addition to the caveats associated with this equation previously discussed for graphene, there is the compounding factor that MoS₂ is not a monoatomic material, suggesting a more complex nature between its defects and its Raman spectrum. The reason for the calculation of $L_{D(est)}$ is that Mignuzzi *et al.* make an implicit assumption that each ion causes one defect. However, unlike in the work of Lucchese *et al.* where ions of much lower energy were used, this is not a safe assumption for either the 25 keV Mn⁺ used by Mignuzzi *et al.* or indeed the 30 keV ions used in this work. As a result, the discussion is not of a physical defect per ion value similar to α_C for graphene. Instead a simpler corrective factor, α_{MoS_2} , is used to bring agreement between the different ions of this work and that of Mignuzzi *et al.*. It is defined as follows:

$$\alpha_{MoS_2} = \frac{L_{D(exp)}^2}{L_{D(est)}^2} \quad (6)$$

The quoted values for α_{MoS_2} are calculated from five mid range data points in order to avoid both the effects of material ablation and intrinsic defects at the high and low dose extremes respectively. The quoted uncertainty is calculated from the corresponding standard deviation. Different values were obtained depending on whether the calculation was based on the E' peak ($\alpha_{E'}$) or the A'_1 peak ($\alpha_{A'_1}$) and these were also averaged (α_{Avg}). All

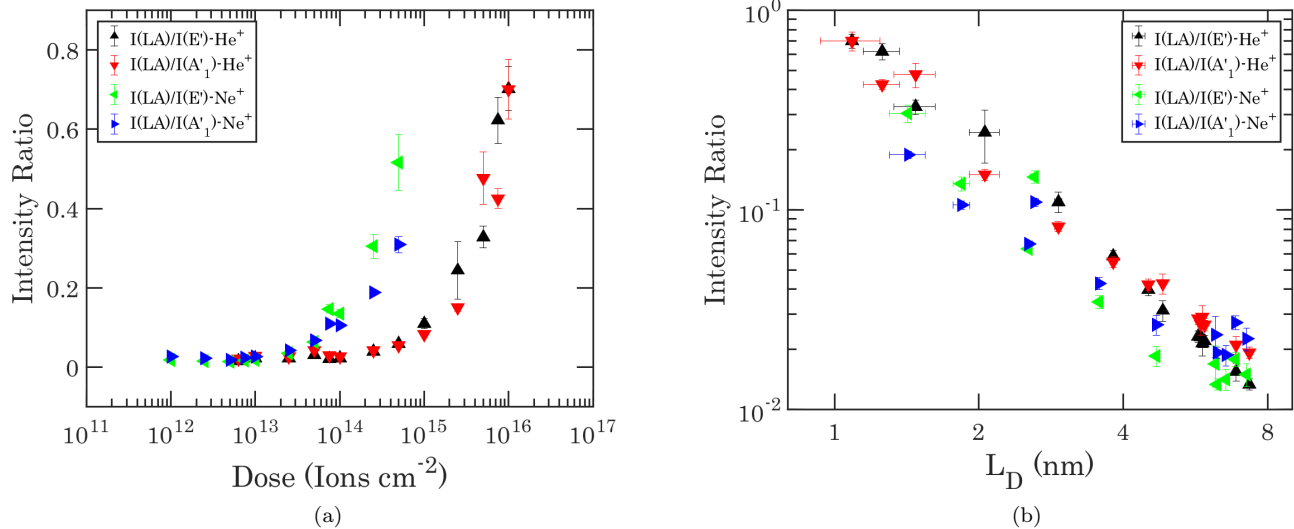


FIG. 6. Evolution of the ratios of the intensity of the LA(M) peak to the intensity of the E' and A'_1 modes for both He^+ and Ne^+ irradiated MoS_2 . (a) plots these ratios against ion dose and (b) plots the same ratios but against L_D (the values of which are calculated as described in the main text).

(a)	γ_{Mo}	γ_S	γ_{MoS_2}
He^+	0.010	0.041	0.030
Ne^+	0.202	0.962	0.709

(b)	$\alpha_{E'}$	$\alpha_{A'_1}$	$\alpha_{Avg.}$
He^+	0.008 ± 0.002	0.012 ± 0.003	0.010 ± 0.002
Ne^+	0.123 ± 0.031	0.196 ± 0.062	0.145 ± 0.035

TABLE III. (a) Calculated sputter yields from SRIM and (b) factors used to correct L_D from the fitting of equation 3 to experimental data as in figure 6.

three are displayed for both ions in table III. SRIM or even atomistic calculated sputter yields are not expected to agree with these results, because unlike in the case of graphene, there is no “one ion per sputtered atom” reference in literature to which our calculated L_D can be matched. Nonetheless, values for sputter yield for S atoms, γ_S , and Mo atoms, γ_{Mo} , are provided from SRIM as well as a weighted average for MoS_2 , γ_{MoS_2} , for reference purposes. For both materials, doses above approximately $5 \times 10^{15} \text{ He}^+ \text{ cm}^{-2}$ or $5 \times 10^{14} \text{ Ne}^+ \text{ cm}^{-2}$ have resulted in severe changes in the spectra to the extent that little or no resemblance is borne to the starting material. For both materials, this severe breakdown occurs at a Ne^+ dose which is between one and two orders of magnitude less than that of He^+ .

IV. CONCLUSION

In this study, the effects of both He^+ and Ne^+ irradiation at 30 keV on graphene and MoS_2 have been explored using models of their Raman spectra. We believe this represents the first experimental comparison of defect sizes produced in 2D materials by different noble gas ion probes. The dose dependence of irradiation species and arrangements to interdefect distance has been established for graphene. A clear comparison to literature is also reported for MoS_2 . In addition, a comparison of the sizes of the defects produced demonstrates the effects of both ion species and secondary, substrate atoms in graphene. The effects of substrate atoms on defect production and size are also highlighted as a concern for nanofabrication technology due to the clear secondary atom effect. These results will allow a substantially better informed and more precise defect engineering of the investigated monolayer materials.

V. ACKNOWLEDGEMENTS

We thank the staff at the Photonics and Advanced Microscopy Laboratories (AML), CRANN, Trinity College Dublin and at the National Laboratory of Solid State Microstructures, Nanjing University. We acknowledge support from the following grants: Science Foundation Ireland [grant numbers: 12/RC/2278, 11/PI/1105, 07/SK/I1220a, and 08/CE/I1432].

- * Corresponding author E-mail: Hongzhou.Zhang@tcd.ie
- ¹ K. S. Novoselov, A. K. Geim, S. V. Morozov, D. Jiang, Y. Zhang, S. V. Dubonos, I. V. Grigorieva, and A. A. Firsov, *Science* **306**, 666 (2004).
 - ² K. S. Novoselov, V. I. Fal'ko, L. Colombo, P. R. Gellert, M. G. Schwab, and K. Kim, *Nature* **490**, 192 (2012).
 - ³ S. Z. Butler, S. M. Hollen, L. Cao, Y. Cui, J. A. Gupta, H. R. Gutie, T. F. Heinz, S. S. Hong, J. Huang, A. F. Ismach, E. Johnston-halperin, M. Kuno, V. V. Plashnitsa, R. D. Robinson, R. S. Ruoff, S. Salahuddin, J. Shan, L. Shi, O. M. G. Spencer, M. Terrones, W. Windl, and J. E. Goldberger, *ACS Nano* **7**, 2898 (2013).
 - ⁴ R. Mas-Ballesté, C. Gómez-Navarro, J. Gómez-Herrero, and F. Zamora, *Nanoscale* **3**, 20 (2011).
 - ⁵ C. Backes, R. J. Smith, N. McEvoy, N. C. Berner, D. McCloskey, H. C. Nerl, A. O'Neill, P. J. King, T. Higgins, D. Hanlon, N. Scheuschner, J. Maultzsch, L. Houben, G. S. Duesberg, J. F. Donegan, V. Nicolosi, and J. N. Coleman, *Nature communications* **5**, 4576 (2014).
 - ⁶ A. Splendiani, L. Sun, Y. Zhang, T. Li, J. Kim, C.-Y. Chim, G. Galli, and F. Wang, *Nano letters* **10**, 1271 (2010).
 - ⁷ K. F. Mak, C. Lee, J. Hone, J. Shan, and T. F. Heinz, *Physical Review Letters* **105**, 136805 (2010).
 - ⁸ C. Lee, H. Yan, L. E. Brus, T. F. Heinz, J. Hone, and S. Ryu, *ACS Nano* **4**, 2695 (2010).
 - ⁹ C. Ataca, H. Sahin, E. Akturk, and S. Ciraci, *The Journal of Physical Chemistry C* **115**, 3934 (2011).
 - ¹⁰ M. Ghorbani-Asl, N. Zibouche, M. Wahiduzzaman, A. F. Oliveira, A. Kuc, and T. Heine, *Scientific reports* **3**, 2961 (2013).
 - ¹¹ Y.-B. Zhou, Z.-M. Liao, Y.-F. Wang, G. S. Duesberg, J. Xu, Q. Fu, X.-S. Wu, and D.-P. Yu, *The Journal of chemical physics* **133**, 234703 (2010).
 - ¹² W. Zhou, X. Zou, S. Najmaei, Z. Liu, Y. Shi, J. Kong, J. Lou, P. M. Ajayan, B. I. Yakobson, and J. C. Idrobo, *Nano Letters* **13**, 2615 (2013).
 - ¹³ M. M. Lucchese, F. Stavale, E. H. M. Ferreira, C. Vilani, M. V. O. Moutinho, R. B. Capaz, C. A. Achete, and A. Jorio, *Carbon* **48**, 1592 (2010).
 - ¹⁴ L. G. Cançado, A. Jorio, E. H. M. Ferreira, F. Stavale, C. A. Achete, R. B. Capaz, M. V. O. Moutinho, A. Lombardo, T. S. Kulmala, and A. C. Ferrari, *Nano Letters* **11**, 3190 (2011).
 - ¹⁵ H.-Q. Zhao, X. Mao, D. Zhou, S. Feng, X. Shi, Y. Ma, X. Wei, and Y. Mao, *Nanoscale* **7**, 7126 (2016).
 - ¹⁶ M. Nastasi, J. W. Mayer, and H. J. K., in *Ion-Solid Interactions: Fundamentals and Applications* (Cambridge University Press, 1996) p. 6287.
 - ¹⁷ D. C. Bell, M. C. Lemme, L. a. Stern, J. R. Williams, and C. M. Marcus, *Nanotechnology* **20**, 455301 (2009).
 - ¹⁸ N. Kalhor, S. a. Boden, and H. Mizuta, *Microelectronic Engineering* **114**, 70 (2014).
 - ¹⁹ D. S. Fox, Y. Zhou, P. Maguire, A. O'Neill, C. O'Coileain, R. Gatensby, A. M. Glushenkov, T. Tao, G. S. Duesberg, I. V. Shvets, M. Abid, M. Abid, H. C. Wu, Y. Chen, J. N. Coleman, J. F. Donegan, and H. Zhang, *Nano Letters* **15**, 5307 (2015).
 - ²⁰ Y. Naitou, T. Iijima, and S. Ogawa, *Applied Physics Letters* **106**, 1 (2015).
 - ²¹ B. S. Archanjo, B. Fragneaud, L. Gustavo Cançado, D. Winston, F. Miao, C. Alberto Achete, and G. Medeiros-Ribeiro, *Applied Physics Letters* **104**, 193114 (2014).
 - ²² R. R. Nair, M. Sepioni, I.-L. Tsai, O. Lehtinen, J. Keinonen, a. V. Krasheninnikov, T. Thomson, a. K. Geim, and I. V. Grigorieva, *Nature Physics* **8**, 199 (2012).
 - ²³ A. Nipane, D. Karmakar, N. Kaushik, S. Karande, and S. Lodha, *ACS Nano* **10**, 2128 (2016).
 - ²⁴ S. Mignuzzi, A. J. Pollard, N. Bonini, B. Brennan, I. S. Gilmore, M. A. Pimenta, D. Richards, and D. Roy, *Physical Review B - Condensed Matter and Materials Physics* **91**, 1 (2015).
 - ²⁵ A. J. Pollard, B. Brennan, H. Stec, B. J. Tyler, M. P. Seah, I. S. Gilmore, and D. Roy, *Applied Physics Letters* **105** (2014), 10.1063/1.4905128.
 - ²⁶ G. Nanda, S. Goswami, K. Watanabe, T. Taniguchi, and P. F. A. Alkemade, *Nano Letters* **15**, 4006 (2015).
 - ²⁷ R. Beams, L. G. Cançado, and L. Novotny, *Nano Letters* **11**, 1177 (2011).
 - ²⁸ A. C. Ferrari, J. C. Meyer, V. Scardaci, C. Casiraghi, M. Lazzeri, F. Mauri, S. Piscanec, D. Jiang, K. S. Novoselov, S. Roth, and A. K. Geim, *Physical Review Letters* **97**, 1 (2006).
 - ²⁹ A. C. Ferrari, *Solid State Communications* **143**, 47 (2007).
 - ³⁰ A. C. Ferrari and D. M. Basko, *Nature Nanotechnology* **8**, 235 (2013).
 - ³¹ F. Tuinstra and J. L. Koenig, *The Journal of Chemical Physics* **53**, 1126 (1970).
 - ³² S. Hang, Z. Moktadir, and H. Mizuta, *Carbon* **72**, 233 (2014).
 - ³³ L. M. Malard, M. A. Pimenta, G. Dresselhaus, and M. S. Dresselhaus, *Physics Reports* **473**, 51 (2009).
 - ³⁴ D. Fox, Y. B. Zhou, A. O'Neill, S. Kumar, J. J. Wang, J. N. Coleman, G. S. Duesberg, J. F. Donegan, and H. Z. Zhang, *Nanotechnology* **24**, 1 (2013).
 - ³⁵ M. O'Brien, N. McEvoy, T. Hallam, H.-Y. Kim, N. C. Berner, D. Hanlon, K. Lee, J. N. Coleman, and G. S. Duesberg, *Scientific Reports* **4**, 7374 (2014).
 - ³⁶ M. Wojdyr, *Journal of Applied Crystallography* **43**, 1126 (2010).
 - ³⁷ M. Wojdyr, "Curve Fitting: Nonlinear Optimization," (2016).
 - ³⁸ F. H. M. Rahman, S. McVey, L. Farkas, J. a. Notte, S. Tan, and R. H. Livengood, *Scanning* **34**, 129 (2012).
 - ³⁹ O. Lehtinen, J. Kotakoski, A. V. Krasheninnikov, A. Tolvanen, K. Nordlund, and J. Keinonen, *Physical Review B* **81**, 153401 (2010).
 - ⁴⁰ O. Lehtinen, J. Kotakoski, a. V. Krasheninnikov, and J. Keinonen, *Nanotechnology* **22**, 175306 (2011).
 - ⁴¹ S. Zhao, J. Xue, Y. Wang, and S. Yan, *Nanotechnology* **23**, 285703 (2012).
 - ⁴² J. F. Ziegler, J. P. Biersack, and U. Littmark, "The Stopping and Range of Ions in Matter," (1985).
 - ⁴³ J. F. Ziegler, M. D. Ziegler, and J. P. Biersack, *Nuclear Instruments and Methods in Physics Research Section B: Beam Interactions with Materials and Atoms* **268**, 1818 (2010).
 - ⁴⁴ J. F. Ziegler, J. P. Biersack, and M. D. Ziegler, *Stopping and Range of Ions in Matter*, 5th ed. (Chester, MD: SRIM Co., 2008).

- ⁴⁵ J. J. Lopez, F. Greer, and J. R. Greer, *Journal of Applied Physics* **107**, 104326 (2010).
- ⁴⁶ J. Orloff, M. Utlaut, and L. Swanson, *High Resolution Focused Ion Beams: FIB and its Applications* (Kluwer/Plenum, New York, NY, 2003).
- ⁴⁷ A. V. Krasheninnikov, *Phenomena in Carbon Nanotubes*.
- ⁴⁸ J. Buchheim, R. M. Wyss, I. Shorubalko, and H. G. Park, *Nanoscale* **8**, 8345 (2016).
- ⁴⁹ G. Gawlik, P. Ciepielewski, J. Jagielski, and J. Baranowski, *Nuclear Instruments and Methods in Physics Research Section B: Beam Interactions with Materials and Atoms* (article i (2017), 10.1016/j.nimb.2017.04.054).
- ⁵⁰ H. Li, Q. Zhang, C. C. R. Yap, B. K. Tay, T. H. T. Edwin, A. Olivier, and D. Baillargeat, *Advanced Functional Materials* **22**, 1385 (2012).
- ⁵¹ C. V. Ramana, U. Becker, V. Shutthanandan, and C. M. Julien, *Geochemical transactions* **9**, 8 (2008).
- ⁵² T. Livneh and J. E. Spanier, *2D Materials* **2**, 035003 (2015).
- ⁵³ M. Ye, D. Winslow, D. Zhang, R. Pandey, and Y. Yap, *Photonics* **2**, 288 (2015).
- ⁵⁴ K. F. Mak, K. He, J. Shan, and T. F. Heinz, *Nature Nanotechnology* **7**, 494 (2012).
- ⁵⁵ M. Barkelid, A. M. Goossens, V. E. Calado, and H. S. J. V. D. Zant, *Nano letters* **12**, 3187 (2012).
- ⁵⁶ C. Rice, R. J. Young, R. Zan, U. Bangert, D. Wolverson, T. Georgiou, R. Jalil, and K. S. Novoselov, *Physical Review B - Condensed Matter and Materials Physics* **87**, 1 (2013).
- ⁵⁷ A. McCreary, R. Ghosh, M. Amani, J. Wang, K. A. N. Duerloo, A. Sharma, K. Jarvis, E. J. Reed, A. M. Dongare, S. K. Banerjee, M. Terrones, R. R. Namburu, and M. Dubey, *ACS Nano* **10**, 3186 (2016).
- ⁵⁸ X. Zhang, W. P. Han, J. B. Wu, S. Milana, Y. Lu, Q. Q. Li, A. C. Ferrari, and P. H. Tan, *Physical Review B - Condensed Matter and Materials Physics* **87**, 1 (2013).
- ⁵⁹ G. L. Frey, R. Tenne, M. J. Matthews, M. S. Dresselhaus, and G. Dresselhaus, *Physical Review B* **60**, 2883 (1999).
- ⁶⁰ A. Zandiatashbar, G.-H. Lee, S. J. An, S. Lee, N. Mathew, M. Terrones, T. Hayashi, C. R. Picu, J. Hone, and N. Koratkar, *Nature Communications* **5**, 3186 (2014).
- ⁶¹ S. Mathew, T. K. Chan, D. Zhan, K. Gopinadhan, A. R. Barman, M. B. H. Breese, S. Dhar, Z. X. Shen, T. Venkatesan, and J. T. L. Thong, *Carbon* **49**, 1720 (2011).
- ⁶² E. H. Ahlgren, J. Kotakoski, O. Lehtinen, and A. V. Krasheninnikov, *Applied Physics Letters* **100** (2012), 10.1063/1.4726053.
- ⁶³ A. Merrill, C. D. Cress, J. E. Rossi, N. D. Cox, and B. J. Landi, *Physical Review B - Condensed Matter and Materials Physics* **92**, 1 (2015).
- ⁶⁴ J. C. Meyer, F. Eder, S. Kurasch, V. Skakalova, J. Kotakoski, H. J. Park, S. Roth, A. Chuvilin, S. Eyhusen, G. Benner, A. V. Krasheninnikov, and U. Kaiser, *Physical Review Letters* **108**, 196102 (2012).
- ⁶⁵ A. Dimiev, D. V. Kosynkin, A. Sinitskii, A. Slesarev, Z. Sun, and J. M. Tour, *Science* **331**, 1168 (2011).
- ⁶⁶ T. C. Nguyen, M. Otani, and S. Okada, *Physical Review Letters* **106**, 1 (2011).
- ⁶⁷ C.-T. Pan, J. a. Hinks, Q. M. Ramasse, G. Greaves, U. Bangert, S. E. Donnelly, and S. J. Haigh, *Scientific reports* **4**, 6334 (2014).
- ⁶⁸ H. P. Komsa, J. Kotakoski, S. Kurasch, O. Lehtinen, U. Kaiser, and A. V. Krasheninnikov, *Physical Review Letters* **109**, 1 (2012).
- ⁶⁹ T. M. McEvoy and K. J. Stevenson, *Langmuir* **21**, 3529 (2005).
- ⁷⁰ M. A. Camacho-López, L. Escobar-Alarcón, M. Picquart, R. Arroyo, G. Córdoba, and E. Haro-Poniatowski, *Optical Materials* **33**, 480 (2011).
- ⁷¹ P. Qin, G. Fang, W. Ke, F. Cheng, Q. Zheng, J. Wan, H. Lei, and X. Zhao, *Journal of Materials Chemistry A* **2**, 2742 (2014).
- ⁷² M. Diskus, O. Nilsen, H. Fjellvag, S. Diplas, P. Beato, C. Harvey, E. van Schroyen Lantman, and B. M. Weckhuysen, *Journal of Vacuum Science & Technology A Vacuum Surfaces and Films* **30** (2012).
- ⁷³ L. Yang, L. Liu, Y. Zhu, X. Wang, and Y. Wu, *Journal of Materials Chemistry* **22**, 13148 (2012).
- ⁷⁴ B. Lafuente, R. T. Downs, H. Yang, and N. Stone, *Highlights in Mineralogical Crystallography* (2015) pp. 1–29.
- ⁷⁵ X. Zhang, X.-F. Qiao, W. Shi, J.-B. Wu, D.-S. Jiang, and P.-H. Tan, *Chem. Soc. Rev.* **44**, 2757 (2015).